AVS Quantum Science

RESEARCH ARTICLE | JULY 30 2026

Mach–Zehnder interferometer for characterization of atom traps

A. Wolf; M. A. Efremov

AVS Quantum Sci. 8, 034401 (2026)
https://doi.org/10.1116/5.0341006

Mach–Zehnder interferometer for characterization of atom traps

Cite as: AVS Quantum Sci. **8**, 034401 (2026); doi: 10.1116/5.0341006
Submitted: 28 April 2026 · Accepted: 9 July 2026 ·
Published Online: 30 July 2026

View Online Export Citation CrossMark

A. Wolf[1,2,a)] and M. A. Efremov[1,2]

AFFILIATIONS

[1]German Aerospace Center (DLR), Institute of Quantum Technologies, 89081 Ulm, Germany
[2]Institut für Quantenphysik and Center for Integrated Quantum Science and Technology (IQST), Universität Ulm, 89069 Ulm, Germany

Note: This paper is part of the Special Topic on Advances in Matter Wave Optics.
[a)]**Electronic mail:** a.wolf@dlr.de

ABSTRACT

Standard characterization of atomic traps relies on tracking classical trajectories, which is limited by the imaging resolution, the amplitude of the oscillation inside the trap, and the lifetime of the gas. We introduce a Mach–Zehnder interferometer technique that overcomes these bottlenecks by mapping the trap frequency ω directly onto internal state populations, which exhibit sharp interference revivals. Yielding an estimated relative uncertainty of $\Delta\omega/\omega = 4.3 \times 10^{-6}$ in 100 ms, this approach extracts precise frequencies and anharmonicity bounds well within typical experimental lifetimes. This efficient calibration enables optimizing atom lenses in delta-kick collimation, advancing inertial sensing, and controlling many-body systems via confinement-induced resonances.

I. INTRODUCTION

The possibility to control the motion of ultracold atoms with magnetic or laser-generated potentials has given rise to the field of atomtronics[1] and the realization of guided atom interferometers.[2–15] Trapping atoms either for some part of [4–6] or for the entire interferometric sequence[3,7–16] increases momentum transfer,[6,11] enclosed area,[6,13–15] and interrogation time,[3–5] making the interferometer highly sensitive to external fields and rotations while allowing for miniaturization.[15] Consequently, the precise control and accurate characterization of these guiding potentials are key issues[1] for improving interferometer performance.

Atoms can be confined using optical dipole[17] or magnetic traps,[18] including atom chips.[19–21] Currently, the standard methods to measure trap frequencies and anharmonicities rely on tracking the classical oscillatory trajectory of atoms inside the trap[7,12,15,22,23] or measuring the response of the trapped gas to parametric heating.[24–27] However, extracting high-precision parameters based on classical dynamics requires observing the atoms with either high spatial resolution, large amplitudes, or over many oscillation periods. In practice, achieving high resolutions is technically demanding, large amplitudes are inaccessible in tight traps, and long observation times clash with the restricted lifetime of cold gases.

In this paper, we overcome these limitations by extracting the trapping frequency directly from sharp interference revivals in an in-trap Mach–Zehnder interferometer (MZI). Rather than tracking macroscopic trajectories of the atomic center-of-mass, we exploit the periodic overlap of wavepackets at integer multiples of the trap period, which manifests as steep crossings at half-population in the output signal. Resolving these times substantially improves the determination of the trapping frequency and anharmonicity bounds well within typical lifetimes. This efficient and fast characterization is essential for optimizing atom lenses in delta-kick collimation, advancing inertial sensing, and controlling atomic interactions via confinement-induced resonances.[28–31]

II. SCHEME IN ONE DIMENSION

We present a method to measure the trap frequencies by means of the atomic MZI depicted in Fig. 1. The scheme requires an atom with two trapped internal states $|\alpha\rangle$, $\alpha = 1, 2$ that have different minima of the trapping potentials. This is the case for the state-dependent potentials $V_\alpha(z) = m\omega_\alpha^2 z^2/2 - F_\alpha z$, consisting of a harmonic trap and a constant force, where either the two frequencies ω_α or the two forces F_α have to differ, for the trap minima at $z_{0,\alpha} = F_\alpha/(m\omega_\alpha^2)$ to be separated. Examples include two trapped states in a magnetic trap

($\omega_1 \neq \omega_2$) with a gravitational sag ($F_1 = F_2$) and two differently levitated states ($F_1 \neq F_2$) in an optical dipole trap ($\omega_1 \approx \omega_2$).

An atomic cloud is initially prepared at rest in the state $|2\rangle$ and, thus, sees the potential $V_2(z)$, shown by the solid line in Fig. 1. At $t = 0$, a short Rabi pulse populates the state $|1\rangle$ and creates a new wavepacket that starts to move in the potential $V_1(z)$, shown by the dashed line in Fig. 1. Since $V_1(z)$ and $V_2(z)$ are confining potentials, the two wavepackets periodically overlap and can be brought to interfere with each other by again transferring population between the states. The trap frequencies are extracted from the measured populations of the internal states after the last pulse, $t = 2T$, Fig. 1.

In the MZI, each wavepacket spends the same amount of time T in both states due to the central π-pulse, at $t = T$, which inverts the population of the states. Consequently, the MZI is insensitive to the ground-state energy of each harmonic potential or any static background field. Moreover, due to the periodic motion alone, no momentum kicks are required to achieve spatial separation and recombination of the wavepackets. Hence, population transfer between the internal states can be realized with radio frequency fields or with co-propagating beams in the microwave regime via Raman transitions, leading to negligible momentum transfer during pulses.

To model the one-dimensional (1D) MZI, we approximate the pulses as instantaneous perfect transfers of the population and assume the initial state to be the Gaussian ground state of the potential $V_2(z)$. The Gaussian wavepackets evolve according to the Newton and Ermakov equations for their center-of-mass position $q(t)$ and width $\sigma(t)$, respectively.[32] The population of state $|2\rangle$ after the last pulse then reads

$$P_2(T) = \frac{1}{2}\left\{1 + C(T)\cos[\varphi(T) + \Delta\Phi_{\mathrm{P}}]\right\}. \tag{1}$$

The contrast $C(T)$ and phase $\varphi(T)$ are defined via the overlap $C(T)\mathrm{e}^{\mathrm{i}\varphi(T)} = \int \mathrm{d}z\,\psi_{\mathrm{u}}^{*}(z, 2T)\psi_{\mathrm{l}}(z, 2T)$ of the two wavepackets at the last pulse, $t = 2T$. The phase $\Delta\Phi_{\mathrm{P}}$ is the difference of two phases imprinted onto the two arms of the MZI during the pulses. More details on the analytic results are summarized in Appendixes A and B.

When the positions of the wavepackets at the last pulse, $t = 2T$, Fig. 2(a), are farther apart than the respective widths, Fig. 2(b), there is no significant overlap and the contrast drops to zero. In this case, the interferometer signal, Eq. (1), flattens at $P_2(T) = 0.5$, as seen in Fig. 2(c) for $4\,\mathrm{ms} < T < 8\,\mathrm{ms}$. However, the signal (thin orange line) displays a peak when T is close to an integer number of the trap periods $\mathcal{T}_1 = 2\pi/\omega_1$ and $\mathcal{T}_2 = 2\pi/\omega_2$ (vertical lines). At these times, both the positions $q_l(2\mathcal{T}_\alpha)$, $q_u(2\mathcal{T}_\alpha)$ and widths $\sigma_l(2\mathcal{T}_\alpha)$, $\sigma_u(2\mathcal{T}_\alpha)$ of the wavepackets coincide, i.e., the interferometer perfectly closes.[33] The widths of the peaks scale quadratically in the distance $|z_{0,2} - z_{0,1}|$ and become narrower for larger separations because the wavepackets spend more time of a period apart.

The two types of peaks at $\mathcal{T}_1$ and $\mathcal{T}_2$ originate from two different trajectories. Figure 1 depicts the case $T = 13.5\,\mathrm{ms}$, which is slightly smaller than $\mathcal{T}_1 \approx 14.14\,\mathrm{ms}$. For $T = \mathcal{T}_1$, the π-pulse is applied when the motion of the upper arm (blue) is at its turning point in the trap

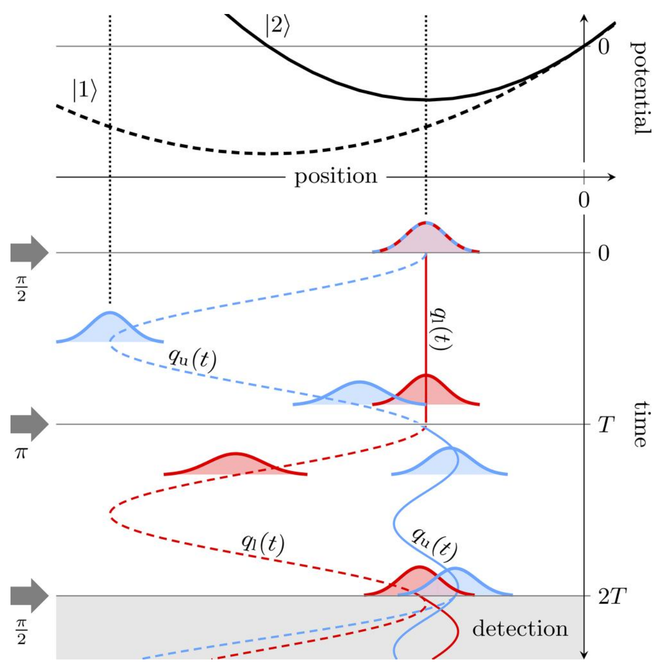

Fig. 1. (Top) Harmonic trapping potentials of two internal states $|1\rangle$ (dashed) and $|2\rangle$ (solid) with spatial shift between the trap centers (minima). (Bottom) Interferometer pulses (thick arrows) separated by time T transfer atoms between the two states, automatically leading to moving and, generally, breathing wavepackets. The shown Mach–Zehnder configuration leads to a periodic two-path-interference of an upper (blue) and lower (red) wavepacket whenever the positions q of their center-of-mass are sufficiently close.

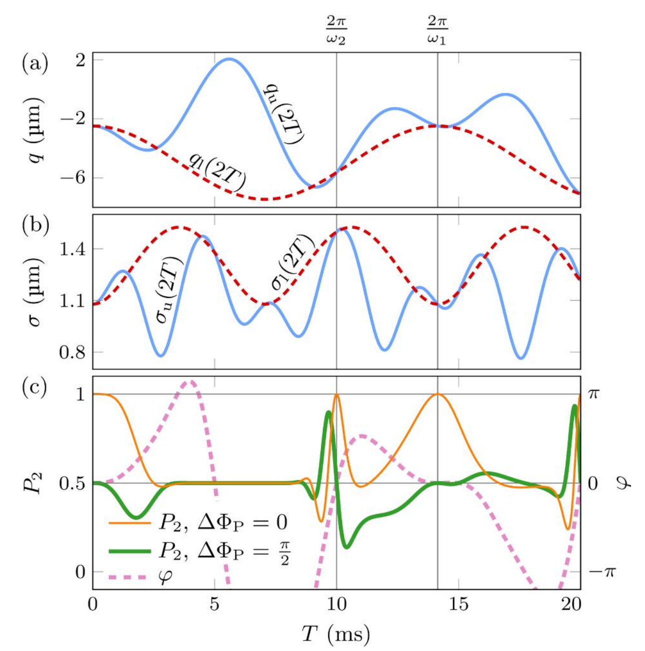

Fig. 2. (a) Positions q and (b) widths σ of the upper (blue solid) and lower (red dashed) wavepackets at the time of the final pulse $2T$ as a function of the time T between the pulses. Here the parameters listed in Table I are used. (c) Signal P_2 of the interferometer for the two pulse phase contributions $\Delta\Phi_{\mathrm{P}} = 0$ (thin orange) and $\Delta\Phi_{\mathrm{P}} = \pi/2$ (thick green). When T matches the trap periods $2\pi/\omega_2 = 10\,\mathrm{ms}$ or $2\pi/\omega_1 \approx 14.14\,\mathrm{ms}$ (vertical lines) the wavepackets are identical at the last pulse and the phase φ (dashed) vanishes.

$V_1(z)$. The atoms are then transferred back to rest in the trap $V_2(z)$, while the lower arm (red) performs the identical motion in $V_1(z)$. Note that if $T = \mathcal{T}_1$, the pulses are always applied when the atoms are back at their initial position. The case of $T = \mathcal{T}_2$ is very different, as the atoms of the upper arm are transferred back to $V_2(z)$, while they are somewhere in motion. However, the interferometer still closes, because the atoms complete one full oscillation in $V_2(z)$ during the second half of the interferometer, while the atoms in the lower arm propagate to the same point.

To determine the period $\mathcal{T}_2$ of the trap in which the atoms are initially prepared, one (i) sets $\Delta\Phi_\mathrm{P} = \pi/2$ and (ii) measures the times T at which the signal crosses the value $P_2(T) = 0.5$ with a large slope. This occurs periodically at $T = n\mathcal{T}_2$ with integer n, as shown in Fig. 2(c) for $n = 1$ (thick green line). We estimate the sensitivity of this approach by expanding contrast and phase around $n\mathcal{T}_2$, $\varphi(T) \approx s(T - n\mathcal{T}_2)$ and $C(T) \approx 1 + \mathcal{O}[(T - n\mathcal{T}_2)^2]$, where the slope

$$s = 4\sin^4\left(\frac{\pi n}{r}\right)\left\{\frac{E}{\hbar}\left[r^2 + \cot^2\left(\frac{\pi n}{r}\right)\right] + \frac{1}{4}\omega_1\frac{(1-r^2)^2}{r}\cot^2\left(\frac{\pi n}{r}\right)\right\} \tag{2}$$

is the sum of a large center-of-mass and small breathing contribution, first and second half, respectively. Here, $r = \omega_2/\omega_1$ and $E = m\omega_1^2(z_{0,2} - z_{0,1})^2/2$ is the energy given to the center-of-mass motion of the upper wavepacket in the first interval. In Appendix C, we derive the relative uncertainty $\Delta\omega_2/\omega_2 = 1/\left(sn\mathcal{T}_2\sqrt{N}\right)$. The sensitivity of our method, therefore, increases for larger slopes s, which is for larger $\sin^4(\pi n/r)$ [Eq. (2)]. For the parameters listed in Table I, the slope s is large at $n = 5$ ($T = 50$ ms) and one obtains $\Delta\omega_2/\omega_2 \approx 4.3 \times 10^{-6}$ with 5000 atoms and 100 shots, i.e., $N = 5 \times 10^5$.

It is instructive to compare this estimation with one for the standard method of tracking the classical motion. In Appendix C, we derive $\Delta\omega/\omega \approx \Delta x/(2\pi nA)$, where A is the amplitude of the oscillation, n is the number of oscillations, and Δx is the uncertainty to determine the position of the atoms. Assuming that the imaging is limited by shot noise, we obtain $\Delta x = \sigma/\sqrt{N}$, with σ being the width of the wavepacket. For our comparison, we take $A = 4$ μm and $\sigma = 1.1$ μm, which corresponds roughly to the motion and initial width of the upper wavepacket in the MZI, as displayed in Figs. 2(a) and 2(b). These values give rise to $\Delta x \approx 1.6$ nm and $\Delta\omega/\omega \approx 6.2 \times 10^{-6}$ using $n = 10$ oscillations. Based on this estimation, the two methods, therefore, look competitive. However, imaging atoms with a precision close to a nanometer is technically challenging. The key advantage of the MZI lies in observing internal state populations in an output port, which is less demanding from an imaging perspective. Nevertheless, in weaker traps, where larger amplitudes A are possible, the required imaging resolution is less restrictive. Alternatively, the number of oscillations n might be increased, though this is ultimately limited by the finite lifetime of the gas.

Our estimations above use 5000 ^{87}Rb atoms. In the degenerate regime, i.e., at temperatures lower than the critical temperature for quantum degeneracy, mean-field interaction effects would play a major role for this number of atoms, especially given the high densities reached in typical atom traps. To preserve the independent-particle dynamics, the MZI should, therefore, be implemented with a collisionless thermal cloud above the critical temperature. Note that this leads to larger cloud widths compared to the one we have used in the single-particle Schrödinger description but does not affect periodic revivals in the interference signal. The interplay between temperature and trap anharmonicities can be problematic because the latter lead to energy-dependent oscillation frequencies.[34] Two atoms at different energies in the thermal cloud, therefore, move at different frequencies, resulting in a loss of contrast. This has been studied theoretically and experimentally before[35] and it was shown that the decrease in contrast is sufficiently small to observe multiple revivals and can be suppressed even further by using an MZI (echo) sequence.

Table I. Parameters of our study case. Here m denotes the mass of ^{87}Rb atom with the typical trapped internal states $|1\rangle = |F=2, m_\mathrm{F}=1\rangle$ and $|2\rangle = |F=2, m_\mathrm{F}=2\rangle$. The applied acceleration $g \equiv F/m$ is in units of the Earth acceleration $g_\mathrm{E} = 9.81\ \mathrm{ms}^{-2}$. With these parameters the initial cloud size in the trap $V_2(z)$ is $\sigma = \sqrt{\hbar/(m\omega_{2,z})} \approx 1.08$ μm.

Axis	$\omega_2/(2\pi)$ (Hz)	$\omega_1/(2\pi)$ (Hz)	F_1	F_2	g/g_E
z	100	$100/\sqrt{2}$	$-mg$	$-mg$	0.1
x	177.77	$177.77/\sqrt{2}$	0	0	⋯
y	277.77	$277.77/\sqrt{2}$	0	0	⋯

III. EXTENSION TO THREE DIMENSIONS

We generalize our scheme to a three-dimensional (3D) scenario where the trapping potentials are separated by a non-zero distance along one axis. This is achieved by aligning the force with one of the trap's principal axes, resulting in the potential $V_\alpha(\mathbf{x}) = \sum_{i=1}^{3} m\omega_{\alpha,x_i}^2 x_i^2/2 - F_\alpha z$ with $\mathbf{x} = (x_1, x_2, x_3) = (x, y, z)$.[36] The contrast $C(T) = C_x(T)C_y(T)C_z(T)$ and the phase $\varphi(T) = \varphi_x(T) + \varphi_y(T) + \varphi_z(T)$ are then given by the contrasts $C_{x_i}(T)$ and the phases $\varphi_{x_i}(T)$, describing the one-dimensional contribution of the x_i-direction.

Our 1D scheme to measure the period $\mathcal{T}_2 = 2\pi/\omega_{2,z}$ in the longitudinal direction z becomes problematic, when the breathing motion of the atomic cloud in the transversal directions x or y has a different periodicity compared to the z direction. For example, if both $\omega_{1,x} \neq \omega_{2,x}$ and $\omega_{1,x} \neq \omega_{1,z}$, the revivals of the contrast are not perfect anymore, because even when the interferometer is closed along the z-direction, it is not closed in the transversal directions, since at $T = n\mathcal{T}_2$, $C_z(n\mathcal{T}_2) = 1$, but $C_{x,y}(n\mathcal{T}_2) < 1$ and $\varphi_{x,y}(n\mathcal{T}_2) \neq 0$. In Fig. 3, the signal $P_2(T)$ of the 3D MZI (solid lines) is contrasted to the one of the 1D MZI (dashed line). For $T = 5\mathcal{T}_2$, $P_2(T) \neq 0.5$ due to

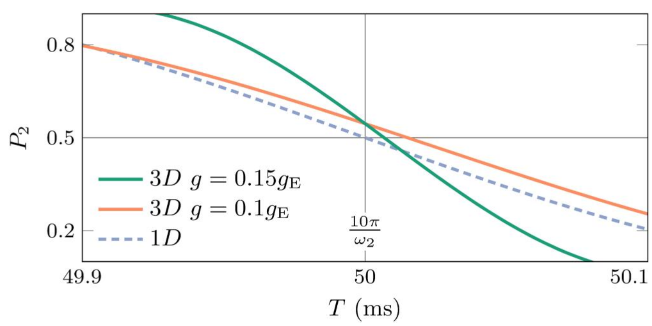

Fig. 3. Signal P_2 of the 1D and 3D MZI for the time T close to $10\pi/\omega_2$. The parameters listed in Table I and the phase difference $\Delta\Phi_\mathrm{P} = \pi/2$ are used.

the nonzero phases coming from the transversal breathing motion. This is not easily accounted for since the phases depend on unknown transversal trap frequencies.

A solution to this problem is repeating the experiment with two different magnitudes of the applied forces, corresponding to different separations $|z_{0,2} - z_{0,1}|$ between the longitudinal traps, and determining the time T when the two signals cross, as shown in Fig. 3. This should occur at $T = n\mathcal{T}_2$, because $C_{x,y}(T)$ and $\varphi_{x,y}(T)$ are independent of the applied forces, while the slope s_{CM}, Eq. (2), with which $\varphi_z(T)$ approaches zero at $T = n\mathcal{T}_2$, scales as $(z_{0,2} - z_{0,1})^2$.

IV. PULSE EFFECTS

Two important aspects were neglected earlier by using perfect instantaneous pulses. First, the nonzero times τ_π and $\tau_{\pi/2}$ of the π- and $\pi/2$-pulses result in a total propagation time $2T + 2\tau_{\pi/2} + \tau_\pi$. This leads to a small systematic horizontal shift of the whole signal. With the method presented above, it is sufficient to determine two neighboring crossings of the value $P_2(T) = 0.5$. The distance between them then defines the period $\mathcal{T}_2$. Second, because of the potentials $V_1(\mathbf{x})$ and $V_2(\mathbf{x})$, the resonance condition for driving transitions between the two internal states depends on the position of the atom. According to Eq. (2), a larger distance $|z_{0,2} - z_{0,1}|$ raises the slope s_{CM} and, hence, the precision of our method. However, this also increases the position-dependent detuning and makes the π- and $\pi/2$-pulses less efficient.

To investigate the performance of the proposed MZI with respect to the applied forces, we simulate the 3D MZI, using a Rabi-coupled two-level Hamiltonian and box-shaped pulses without pulse phase ($\Delta\Phi_{\mathrm{P}} = 0$), as detailed in Appendix A. The pulses are driven with the frequency such that the transition at the initial position [right vertical dotted line Fig. 1(top)] is resonant. After the first $\pi/2$-pulse, the atoms in $|1\rangle$ start to move and the largest detuning they acquire is at the position of the other turning point [left vertical dotted line Fig. 1(top)]. Subtracting the level splitting $V_2(0,0,z_{0,2}) - V_1(0,0,z_{0,2})$ from $V_2(0,0,2z_{0,1} - z_{0,2}) - V_1(0,0,2z_{0,1} - z_{0,2})$ yields the detuning $\delta = 2(F_2\omega_1^2 - F_1\omega_2^2)^2/(\hbar m\omega_1^4\omega_2^2)$.

For the Rabi frequency $\Omega = 2\pi \times 25\,\mathrm{kHz}$, corresponding to $\tau_{\pi/2} = 10\,\mu\mathrm{s}$ and $\tau_\pi = 20\,\mu\mathrm{s}$, and the parameters listed in Table I, we obtain the small detuning $\delta \approx 0.042\,\Omega$ and Fig. 4(a) shows that the 3D analytic model accurately describes our MZI. However, for an applied force, one order of magnitude larger, i.e., $g = g_{\mathrm{E}}$, the detuning becomes too large, $\delta \approx 4.25\,\Omega$, and the π-pulse fails to exchange the populations between the states $|1\rangle$ and $|2\rangle$. At $T = \mathcal{T}_2$, there are quick suppressed oscillations, Fig. 4(a), due to the large slope, Eq. (2), and greatly reduced contrast. Conversely, at $T = \mathcal{T}_1$, the atoms come back to the initial position, Fig. 1, for all pulses and our analytic model remains very accurate. Hence, for large detunings, an alternative way for extracting the trap frequency is to identify the narrow quasi-Gaussian peaks at $n\mathcal{T}_1$ and determine the time interval between such peaks.

V. APPLICATION TO OPTICAL DIPOLE TRAPS

We now examine the 3D MZI with perfect pulses inside a crossed optical dipole trap. As considered in Appendix D, the trapping potential is modeled as two Gaussian laser beams propagating along the x- and y-axes with wavelength 1064 nm, power 1 W, and beam waist 100 μm.[17] The ^{87}Rb atoms in the trap are pulled downward by

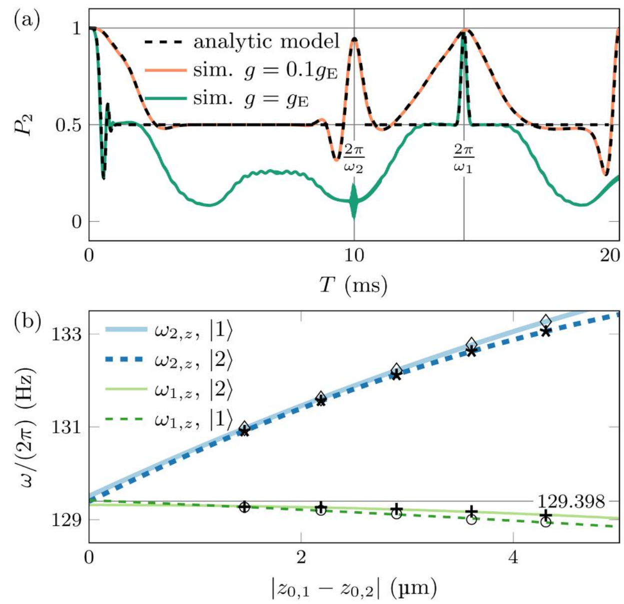

FIG. 4. (a) Interferometer signals P_2 as a function of the pulse separation T. The trap parameters are listed in Table I. Solid lines are simulations of a Rabi-coupled two-level Hamiltonian including the influence of position-dependent detunings. (b) Trap frequencies ω and corresponding fits determined by simulating the 3D MZI inside an optical dipole trap for different trap separations $|z_{0,1} - z_{0,2}|$ and initial states.

gravity with $F_1 = -mg_{\mathrm{E}}$ such that the trap center is at $z_{0,1} \approx -13.72\,\mu\mathrm{m}$ below the focus of the laser beams. Expanding the potential into a Taylor series at $z_{0,1}$ up to the second order results in the trap frequencies $\omega_{1,x} = \omega_{1,y} \approx 2\pi \times 95.15\,\mathrm{Hz}$ and $\omega_{1,z} \approx 2\pi \times 129.398\,\mathrm{Hz}$. Our goal is to determine $\omega_{1,z}$ with the 3D MZI and investigate the influence of small anharmonicities.[37–39] As $|1\rangle$, we choose the magnetically insensitive state $|m_F = 0\rangle$, while as $|2\rangle$, we choose a magnetically sensitive state $|m_F \neq 0\rangle$. In this way, a magnetic field gradient provides the force $F_2 = -mg_2$ with a controllable effective acceleration $g_2 \neq g_{\mathrm{E}}$.

Due to the shape of the optical dipole potential, the trap frequencies experienced by the atoms in state $|2\rangle$ slightly depend on g_2. For example, at $g_2 = 0.7g_{\mathrm{E}}$ we obtain $z_{0,2} \approx -9.42\,\mu\mathrm{m}$, $\omega_{2,x} = \omega_{2,y} \approx 2\pi \times 96.11\,\mathrm{Hz}$, and $\omega_{2,z} \approx 2\pi \times 133.48\,\mathrm{Hz}$. The difference of the transversal frequencies $\omega_{1,x} - \omega_{2,x}$ is too small for the corresponding breathing motion to be important. However, the corresponding difference in the longitudinal ones is large enough for the peaks in the signal $P_2(T)$ to be clearly distinguishable at $90\,\mathrm{ms} < T < 155\,\mathrm{ms}$. Since the interferometer can be started either in $|1\rangle$ or in $|2\rangle$, both trap frequencies $\omega_{1,z}$ and $\omega_{2,z}$ can be independently determined by performing the 3D MZI for $g_2/g_{\mathrm{E}} = 0.7, 0.75, 0.8, 0.85, 0.9$, as displayed in Fig. 4(b). The extraction of the frequencies from the signals is explained in Appendix F. Starting the 3D MZI in the states $|2\rangle$ and $|1\rangle$ gives us slightly different estimates for $\omega_{1,z}$, circles and crosses, and $\omega_{2,z}$, stars and diamonds. Moreover, both frequencies clearly display a dependence on the distance between the trap centers $|z_{0,1} - z_{0,2}|$, that is on g_2. For $\omega_{1,z}$, this entirely originates from small anharmonicities of $V_1(\mathbf{x})$. The frequency $\omega_{2,z}$ has a stronger dependence on the distance because the trap minimum $z_{0,2}$ changes with g_2. As outlined in Appendix E, we use the standard formula for the classical oscillation frequency in the presence of weak anharmonicities to justify the fitting functions (quadratic polynomials) shown by the solid and dashed lines in Fig. 4(b). Extrapolating these lines to $|z_{0,1} - z_{0,2}| = 0$, where the effect of anharmonicities vanishes, and the traps are identical and yields four estimations for $\omega_{1,z}$. These four values give the average $\omega^{\rm av}_{1,z} \approx 2\pi \times 129.408\,{\rm Hz}$ with the relative deviation $1-\omega_{1,z}/\omega^{\rm av}_{1,z} \approx 7.7\times10^{-5}$ to the true value $\omega_{1,z} = 2\pi\times129.398\,{\rm Hz}$. Finally, using the fit of $\omega_{1,z}$ given by the lower (green) solid line, we obtain the upper bounds $|\alpha| < 4.63\times10^{-16}\,{\rm J\,m^{-3}}$ and $|\beta| < 5.63\times10^{-12}\,{\rm J\,m^{-4}}$ for the magnitudes of the cubic α and quartic β anharmonic terms $\alpha(z-z_{0,1})^3$ and $\beta(z-z_{0,1})^4$ in $V_1(\mathbf{x})$. They are consistent with the values $\alpha \approx 2.76\times10^{-16}\,{\rm J\,m^{-3}}$ and $\beta \approx -4.39\times10^{-12}\,{\rm J\,m^{-4}}$ derived with the Taylor expansion.

VI. CONCLUSION

We have proposed an in-trap Mach–Zehnder atom interferometer to determine trapping frequencies by mapping them directly onto sharp revivals of the interferometer signal. Our method yields an estimated relative uncertainty of $\Delta\omega/\omega \approx 4.3\times10^{-6}$ for a trapping frequency of $\omega = 2\pi\times100\,{\rm Hz}$ in $2T = 100\,{\rm ms}$ of interrogation time. For comparison, state-of-the-art ballistic measurements have demonstrated a relative uncertainty of $\Delta\omega/\omega \approx 7.8\times10^{-5}$ for a trapping frequency of $\omega \approx 2\pi\times3.8673\,{\rm Hz}$ but require observation times up to 100 s.[15]

By shifting the measurement from tracking spatial trajectories to an interference signal in populations of internal states, our scheme is less demanding on the imaging technique while achieving high sensitivity in short interrogation times. This efficient calibration provides an essential tool for the optimal design of atomic lenses[40,41] and delta-kick collimation, which are critical for advancing precision atom interferometry[42] and compact inertial sensors. Furthermore, our technique opens new prospects in fundamental quantum science, enabling the precise determination of the thermodynamic properties of trapped Bose–Einstein condensates[43] and paving the way for advanced control of few- and many-body systems via confinement-induced resonances.[28–31]

DEDICATION

We dedicate this work to Professor Dr. Ernst Maria Rasel, a deep-thinking physicist and a wonderful person, on the occasion of his 60th birthday. His pioneering contributions to atom-based quantum sensing, especially in fundamental physics and matter-wave optics, have been a lasting source of inspiration for our research. We extend our warmest wishes and deep appreciation.

ACKNOWLEDGMENTS

The authors gratefully acknowledge W. P. Schleich for fruitful discussions as well as the scientific support and HPC resources provided by the German Aerospace Center (DLR). The HPC system CARA was partially funded by the Saxon State Ministry for Economic Affairs, Labour and Transport and the Federal Ministry for Economic Affairs and Climate Action. The authors acknowledge the support by the state of Baden-Württemberg through bwHPC and the German Research Foundation (DFG) through Grant No. INST 40/575-1 FUGG (JUSTUS 2 cluster). This work was supported by the Science Sphere Quantum Science of Ulm University and the Center for Integrated Quantum Science and Technology (IQST). The research of the IQST was financially supported by the Ministry of Science, Research and Arts Baden-Württemberg.

AUTHOR DECLARATIONS

Conflict of Interest

The authors have no conflicts to disclose.

Author Contributions

A. Wolf: Conceptualization (supporting); Formal analysis (lead); Methodology (lead); Software (lead); Validation (equal); Visualization (lead); Writing – original draft (lead). **M. A. Efremov:** Conceptualization (lead); Formal analysis (supporting); Methodology (supporting); Validation (equal); Visualization (supporting); Writing – review & editing (lead).

DATA AVAILABILITY

The data that support the findings of this study are available from the corresponding author upon reasonable request.

APPENDIX A: ANALYTIC MODEL

A driven two-level atom of mass m in an external state-dependent potential $V_\alpha(\mathbf{x})$, with $\alpha = 1, 2$, is described by the Hamiltonian,

$$H = -\frac{\hbar^2}{2m}\nabla^2\mathbb{1} + V_1(\mathbf{x})|1\rangle\langle1| + V_2(\mathbf{x})|2\rangle\langle2| + \hbar\Omega(t)\cos[\omega_{\rm d}t + \phi(t)]\sigma_x + \frac{\hbar\omega_{\rm b}}{2}\sigma_z \qquad \text{(A1)}$$

with the Rabi frequency $\Omega(t)$ and the driving frequency $\omega_{\rm d}$. Here, $\phi(t)$ denotes the pulse phase and $\hbar\omega_{\rm b}$ is the transition frequency between the internal states $|1\rangle$ and $|2\rangle$. Moreover, $\mathbb{1}$ denotes the identity 2×2 matrix, whereas $\sigma_x = |1\rangle\langle2| + |2\rangle\langle1|$ and $\sigma_z = |2\rangle\langle2| - |1\rangle\langle1|$ are the Pauli matrices. Note that the pulse phase is allowed to be weakly time-dependent $\dot\phi(t) \ll \omega_{\rm d}$. The Rabi frequency is nonzero only during the short pulses. As an example, the results presented in Fig. 4(a) are obtained by using box-shaped pulses, with Ω being a constant and nonzero only in the time intervals: $0 \le t \le 10\,\mu{\rm s}$, $T + 10\,\mu{\rm s} \le {\rm t} \le {\rm T} + 30\,\mu{\rm s}$, and $2T + 30\,\mu{\rm s} \le {\rm t} \le 2{\rm T} + 40\,\mu{\rm s}$.

For typical parameters, there is a separation of timescales between the internal dynamics of the atom and the external dynamics of its center-of-mass motion. This allows us to derive the approximate unitary time-evolution operators describing the action of the pulses by neglecting the first line in the Hamiltonian (A1). Taking the instantaneous pulses and using the rotating wave approximation, these operators for perfect $\pi/2$- and π-pulses are given by

$$U_{\frac{\pi}{2}} = \frac{1}{\sqrt2}\mathbb{1} - \frac{\rm i}{\sqrt2}\left[{\rm e}^{{\rm i}\phi({\rm t})}|2\rangle\langle1| + {\rm e}^{-{\rm i}\phi({\rm t})}|1\rangle\langle2|\right], \qquad \text{(A2)}$$

$$U_\pi = -\mathrm{i}\left[\mathrm{e}^{\mathrm{i}\phi(t)}|2\rangle\langle 1| + \mathrm{e}^{-\mathrm{i}\phi(t)}|1\rangle\langle 2|\right], \tag{A3}$$

where the pulse phase $\phi(t)$ is to be evaluated at the instant of the pulse (0, T, $2T$ in our case). Here, we also assume that there is no detuning.

Let the atom be prepared in the ground state of a harmonic trap and in the internal state $|2\rangle$, giving rise to the total state of the atom $|\Psi(z,0)\rangle = \psi(z,0)|2\rangle$. After the first $\pi/2$-pulse, the state reads $|\Psi(z,0+\varepsilon)\rangle = \psi(z,0)(|2\rangle - \mathrm{i}|1\rangle\mathrm{e}^{-\mathrm{i}\phi(0)})/\sqrt{2}$, where ε is an infinitesimally small number. Due to the different potentials $V_1(z)$ and $V_2(z)$, the *lower* $\psi_\mathrm{l}(z,t)$ and *upper* $\psi_\mathrm{u}(z,t)$ wavepackets evolve independently, as shown in Fig. 1. The state immediately before the π-pulse, therefore, reads $|\Psi(z,T-\varepsilon)\rangle = [\psi_\mathrm{l}(z,T)|2\rangle - \mathrm{i}\psi_\mathrm{u}(z,T)|1\rangle\mathrm{e}^{-\mathrm{i}\phi(0)}]/\sqrt{2}$, where the method to evaluate $\psi_\mathrm{l}(z,T)$ and $\psi_\mathrm{u}(z,T)$ is presented below. Directly after the π-pulse, the state is given by $|\Psi(z,T+\varepsilon)\rangle = -\mathrm{i}\{\psi_\mathrm{l}(z,T)|1\rangle\mathrm{e}^{-\mathrm{i}\phi(\mathrm{T})} - \mathrm{i}\psi_\mathrm{u}(z,T)|2\rangle\mathrm{e}^{-\mathrm{i}[\phi(0)-\phi(\mathrm{T})]}\}/\sqrt{2}$. The state after the last $\pi/2$-pulse reads

$$\begin{aligned}|\Psi(z,2T)\rangle = &-\frac{1}{2}\left[\psi_\mathrm{u}(z,2T)\mathrm{e}^{\mathrm{i}\Phi_{\mathrm{P},1}} + \psi_\mathrm{l}(z,2T)\mathrm{e}^{\mathrm{i}\Phi_{\mathrm{P},2}}\right]|2\rangle\\ &+\frac{\mathrm{i}}{2}\left[\psi_\mathrm{u}(z,2T)\mathrm{e}^{\mathrm{i}\Phi_{\mathrm{P},3}} - \psi_\mathrm{l}(z,2T)\mathrm{e}^{\mathrm{i}\Phi_{\mathrm{P},4}}\right]|1\rangle\end{aligned} \tag{A4}$$

with $\Phi_{\mathrm{P},1} = \phi(T) - \phi(0)$, $\Phi_{\mathrm{P},2} = \phi(2T) - \phi(T)$, $\Phi_{\mathrm{P},3} = \phi(T) - \phi(0) - \phi(2T)$, $\Phi_{\mathrm{P},4} = -\phi(T)$. The pulse phase contribution to the signal, Eq. (1), is $\Delta\Phi_\mathrm{P} = \Phi_{\mathrm{P},2} - \Phi_{\mathrm{P},1} = \phi(0) - 2\phi(T) + \phi(2T)$ and this can be made equal to $\pi/2$ by choosing $\phi(t) = \pi t^2/(4T^2)$. For Fig. 4(a), we have set $\phi(t) = 0$ to have no pulse phase contribution.

APPENDIX B: WAVEPACKET PROPAGATION

A Gaussian wavepacket inside a harmonic potential keeps its Gaussian shape during the time evolution[32] as follows:

$$\psi(z,t) = \frac{1}{\sqrt{\sqrt{\pi}\sigma(t)}}\exp\left\{-\frac{\left[z-q(t)\right]^2}{2\sigma^2(t)}\right\}\mathrm{e}^{\frac{\mathrm{i}}{\hbar}S(z,t)} \tag{B1}$$

with

$$S(z,t) = \frac{1}{2}a(t)\left[z-q(t)\right]^2 + b(t)\left[z-q(t)\right] + c(t). \tag{B2}$$

Inserting this wavefunction into the 1D Schrödinger equation with the potential $V(z) = m\omega^2 z^2/2 - Fz$ and separating real and imaginary part for each order in z yields

$$\ddot{\sigma}(t) + \omega^2\sigma(t) = \frac{\hbar^2}{m^2\sigma^3(t)}, \tag{B3}$$

$$\ddot{q}(t) + \omega^2 q(t) = \frac{F}{m}, \tag{B4}$$

$$a(t) = m\frac{\dot{\sigma}(t)}{\sigma(t)}, \tag{B5}$$

$$b(t) = m\dot{q}(t), \tag{B6}$$

$$\dot{c}(t) = \frac{1}{2}m\dot{q}^2(t) - \frac{1}{2}m\omega^2 q^2(t) + Fq(t) - \frac{\hbar^2}{2m\sigma^2(t)}. \tag{B7}$$

The solution for $q(t)$ and $\sigma(t)$ in terms of their initial values q_0, $\dot{q}_0$ and σ_0, $\dot{\sigma}_0$ is

$$q(t) = \frac{F}{m\omega^2} + \left(q_0 - \frac{F}{m\omega^2}\right)\cos(\omega t) + \frac{\dot{q}_0}{\omega}\sin(\omega t), \tag{B8}$$

$$\begin{aligned}\sigma(t) = \sigma_0\Bigg[&\frac{1}{2}\left(1 + \frac{\dot{\sigma}_0^2}{\omega^2\sigma_0^2} + \frac{\hbar^2}{m^2\omega^2\sigma_0^4}\right) + \frac{\dot{\sigma}_0}{\omega\sigma_0}\sin(2\omega t)\\ &+\frac{1}{2}\left(1 - \frac{\dot{\sigma}_0^2}{\omega^2\sigma_0^2} - \frac{\hbar^2}{m^2\omega^2\sigma_0^4}\right)\cos(2\omega t)\Bigg]^{1/2}\end{aligned} \tag{B9}$$

which determines $a(t)$, $b(t)$, and $c(t)$. The latter splits into a contribution from the classical center-of-mass (CM) motion as follows:

$$\begin{aligned}c_\mathrm{CM}(t) = &\frac{1}{2}m\left[\dot{q}(t)q(t) - \dot{q}_0 q_0\right] + \frac{F^2}{2m\omega^2}t\\ &+\frac{F}{2\omega}\left(q_0 - \frac{F}{m\omega^2}\right)\sin(\omega t)\\ &-\frac{F\dot{q}_0}{2\omega^2}\left[\cos(\omega t) - 1\right]\end{aligned} \tag{B10}$$

and breathing of the wavepacket,

$$\begin{aligned}c_\mathrm{B}(t) = -\frac{\hbar}{2}\Bigg\{&\pi\left\lfloor\frac{1}{2} + \frac{\omega t}{\pi}\right\rfloor - \arctan\left(\frac{m\dot{\sigma}_0\sigma_0}{\hbar}\right)\\ &+\arctan\left[\frac{m\dot{\sigma}_0\sigma_0}{\hbar} + \left(\frac{m\dot{\sigma}_0^2}{\hbar\omega} + \frac{\hbar}{m\omega\sigma_0^2}\right)\tan(\omega t)\right]\Bigg\}\end{aligned} \tag{B11}$$

with the floor function $\lfloor x\rfloor$. Hence, we have $c(t) = c_\mathrm{CM}(t) + c_\mathrm{B}(t) + c_0$, where c_0 can be set zero since any interferometer starts from a single wavepacket that is split apart by pulses. Consequently, all wavepackets share the same c_0 which, therefore, turns into a global phase.

By splitting the overlap $\int \mathrm{d}z\psi_\mathrm{u}^*(z,2T)\psi_\mathrm{l}(z,2T)$ of two Gaussian wavepackets into modulus and phase, we can give formal expressions for the contrast $C(T)$ and phase $\varphi(T)$ of the MZI which likewise split into breathing and CM contributions

$$C_\mathrm{B}(T) = \sqrt{\frac{2}{\sigma_\mathrm{u}(2T)\sigma_\mathrm{l}(2T)}}\frac{1}{\sqrt{|W_\mathrm{l}^*(2T) + W_\mathrm{u}(2T)|}}, \tag{B12}$$

$$\begin{aligned}\varphi_\mathrm{B}(T) = &\frac{1}{2}\arctan\left\{\frac{\mathrm{Im}\left[W_\mathrm{l}^*(2T) + W_\mathrm{u}(2T)\right]}{\mathrm{Re}\left[W_\mathrm{l}^*(2T) + W_\mathrm{u}(2T)\right]}\right\}\\ &+\frac{c_{\mathrm{B,l}}(2T) - c_{\mathrm{B,u}}(2T)}{\hbar},\end{aligned} \tag{B13}$$

$$\begin{aligned}C_\mathrm{CM}(T) = \exp\Bigg\{\mathrm{Re}\Bigg[&-\frac{b_\mathrm{l}^2(2T)}{2\hbar^2 W_\mathrm{l}(2T)} - \frac{b_\mathrm{u}^2(2T)}{2\hbar^2 W_\mathrm{u}^*(2T)}\\ &-\frac{1}{2}\frac{W_\mathrm{l}(2T)W_\mathrm{u}^*(2T)}{W_\mathrm{l}(2T) + W_\mathrm{u}^*(2T)}\left[Q_\mathrm{l}(2T) - Q_\mathrm{u}^*(2T)\right]^2\Bigg]\Bigg\},\end{aligned} \tag{B14}$$

$$
\begin{aligned}
\varphi_{\mathrm{CM}}(T) = \exp\Bigg\{ \mathrm{Im}\Bigg[&-\frac{b_\mathrm{l}^2(2T)}{2\hbar^2 W_\mathrm{l}(2T)} - \frac{b_\mathrm{u}^2(2T)}{2\hbar^2 W_\mathrm{u}^*(2T)} \\
&- \frac{1}{2}\frac{W_\mathrm{l}(2T)W_\mathrm{u}^*(2T)}{W_\mathrm{l}(2T)+W_\mathrm{u}^*(2T)}\left[Q_\mathrm{l}(2T)-Q_\mathrm{u}^*(2T)\right]^2 \Bigg] \\
&+ \frac{c_{\mathrm{CM,l}}(2T)-c_{\mathrm{CM,u}}(2T)}{\hbar} \Bigg\},
\end{aligned} \tag{B15}
$$

respectively. Here, the abbreviations $W(t) = 1/\sigma^2(t) - \mathrm{i}a(t)/\hbar$ and $Q(t) = q(t) + \mathrm{i}b(t)/[\hbar W(t)]$ are used.

To obtain the values of $\sigma(2T)$ and $q(2T)$ for each wavepacket, we have to make ω and F piecewise time-dependent. The scenario in Fig. 1 is given by

$$
\omega_\mathrm{u}(t) = \begin{cases} \omega_1, & 0 < t \le T, \\ \omega_2, & T < t \le 2T, \end{cases} \quad F_\mathrm{u}(t) = \begin{cases} F_1, & 0 < t \le T, \\ F_2, & T < t \le 2T, \end{cases} \tag{B16}
$$

$$
\omega_\mathrm{l}(t) = \begin{cases} \omega_2, & 0 < t \le T, \\ \omega_1, & T < t \le 2T, \end{cases} \quad F_\mathrm{l}(t) = \begin{cases} F_2, & 0 < t \le T, \\ F_1, & T < t \le 2T, \end{cases} \tag{B17}
$$

and since the interferometer starts in the ground state of the trap in state $|2\rangle$, the initial values for the first time interval are

$$
q_{0,\mathrm{u}}^{(1)} = q_{0,\mathrm{l}}^{(1)} = \frac{F_2}{m\omega_2^2}, \tag{B18}
$$

$$
\dot{q}_{0,\mathrm{u}}^{(1)} = \dot{q}_{0,\mathrm{l}}^{(1)} = 0, \tag{B19}
$$

$$
\sigma_{0,\mathrm{u}}^{(1)} = \sigma_{0,\mathrm{l}}^{(1)} = \sqrt{\frac{\hbar}{m\omega_2}}, \tag{B20}
$$

$$
\dot{\sigma}_{0,\mathrm{u}}^{(1)} = \dot{\sigma}_{0,\mathrm{l}}^{(1)} = 0. \tag{B21}
$$

Inserting this information into Eqs. (B8) and (B9) propagates the wavepackets up to $t = T$. This yields the initial conditions for the second time interval where Eqs. (B8) and (B9) have to be modified by setting $t \to t - T$. In this piecewise fashion, we can propagate the wavepackets to the time of the last pulse $t = 2T$ and the action $c(2T)$ accumulated by each wavepacket can be determined in the same way from Eqs. (B10) and (B11). The generalization to the 3D MZI is straightforward by using product wavefunctions $\psi(\mathbf{x}, t) = \prod_i \psi_i(x_i, t)$.

APPENDIX C: ESTIMATING THE RELATIVE UNCERTAINTY

1. Mach–Zehnder interferometer scheme

To estimate the sensitivity of our proposed MZI, we assume the measurement is fundamentally limited by quantum projection noise (atom shot noise). The observable of the interferometer is the population in state $|2\rangle$ at the final time $2T$, given by Eq. (1). If the experiment is performed with N_{atoms} per shot and averaged over N_{shots} independent measurements, the total number of interrogated atoms is $N = N_{\mathrm{atoms}}N_{\mathrm{shots}}$. The fundamental projection noise in the measured population $P_2(T)$ is then given by

$$
\Delta P_2(T) = \sqrt{\frac{P_2(T)[1-P_2(T)]}{N}}. \tag{C1}
$$

On the other hand, applying Gaussian error propagation to the interferometer signal, Eq. (1), yields

$$
\Delta P_2(T) = \sqrt{\left[\frac{\partial P_2(T)}{\partial \omega_2}\right]^2 \Delta\omega_2^2 + \cdots}, \tag{C2}
$$

where the dots indicate contributions from other parameters with nonzero uncertainty. We assume these to be small compared to the one by ω_2 and, therefore, obtain $\Delta P_2(T) \approx |\partial P_2(T)/\partial\omega_2|\Delta\omega_2$. Inserting this result into Eq. (C1), we arrive at

$$
\Delta\omega_2 \approx \frac{1}{\sqrt{N}} \frac{\sqrt{P_2(T)[1-P_2(T)]}}{|\partial P_2(T)/\partial\omega_2|}. \tag{C3}
$$

To maximize the sensitivity, the interferometer is operated at the steepest point of the interference signal. This is achieved in two steps. First, we set the pulse phase contribution to $\Delta\Phi_\mathrm{P} = \pi/2$, which changes the signal, Eq. (1), to $P_2(T) = \{1 - C(T)\sin[\varphi(T)]\}/2$. Second, we choose the interrogation time close to a full revival at $T \approx n\mathcal{T}_2 = 2\pi n/\omega_2$. Expanding phase and contrast around a revival yields $\varphi(T) \approx s(T - n\mathcal{T}_2)$ and $C(T) \approx 1 + \mathcal{O}[(T - n\mathcal{T}_2)^2]$ with the slope s given by Eq. (2). The interferometer signal, therefore, reads

$$
P_2(T) \approx \frac{1}{2}[1 - s(T - n\mathcal{T}_2)], \tag{C4}
$$

leading to

$$
\sqrt{P_2(T)[1-P_2(T)]} \approx \frac{1}{2}, \tag{C5}
$$

$$
\left|\frac{\partial P_2(T)}{\partial\omega_2}\right| \approx \frac{sn\mathcal{T}_2}{2\omega_2}, \tag{C6}
$$

and

$$
\frac{\Delta\omega_2}{\omega_2} \approx \frac{1}{sn\mathcal{T}_2\sqrt{N}}. \tag{C7}
$$

2. Tracking the classical motion

A similar derivation can be done for estimating the sensitivity of tracking the classical motion $x(t) = A\sin(\omega t)$ with amplitude A. Gaussian error propagation method yields $\Delta x(t) \approx |\partial x(t)/\partial\omega|\Delta\omega = At|\cos(\omega t)|\Delta\omega$. Measuring the position of the atoms after n oscillations, which is at $t = 2\pi n/\omega$, therefore, gives rise to $\Delta\omega/\omega \approx \Delta x/(2\pi n A)$. The position uncertainty can be estimated as $\Delta x = \sigma/\sqrt{N}$, assuming that the imaging of the atoms is limited by shot noise. Here, σ is the width of the wavepacket.

APPENDIX D: OPTICAL DIPOLE TRAP MODEL

An alkali atom inside a far-detuned, linearly polarized, monochromatic Gaussian laser beam, with its focus being at the origin of the coordinate system and propagating along the x_i-axis with the intensity,

$$I_i(\mathbf{x}) = \frac{2P_i}{\pi w_i^2(1+x_i^2/R_i^2)}\exp\left[-\frac{2(\mathbf{x}^2-x_i^2)}{w_i^2(1+x_i^2/R_i^2)}\right], \tag{D1}$$

is affected by the optical dipole potential $V_i(\mathbf{x}) = \hbar\kappa I_i(\mathbf{x})/8$ with $\kappa = (\kappa_{D1}+2\kappa_{D2})/3$ and

$$\kappa_D = \frac{12\pi c^2}{\hbar\omega_D^3}\left(\frac{\Gamma_D}{\omega_i-\omega_D}-\frac{\Gamma_D}{\omega_i+\omega_D}\right), \tag{D2}$$

where P_i is the power, w_i is the beam waist, $R_i = \pi w_i^2/\lambda_i$ is the Rayleigh range, λ_i is the wavelength of the laser, $\omega_i = 2\pi c/\lambda_i$ is its frequency, ω_D is the transition frequency of the D-lines D1 and D2, and Γ_D is the corresponding linewidth.[17]

In Sec. V we consider a crossed optical dipole trap where two Gaussian laser beams with the same power P, beam waist w, and wavelength λ have their focus at the origin of our coordinate system. One laser beam propagates along the x-axis and the other one along the y-axis. The total optical dipole potential is, therefore, given by $V_{OD}(\mathbf{x}) = V_x(\mathbf{x}) + V_y(\mathbf{x})$. The wavelength of $\lambda = 1064$ nm is red-detuned with respect to the D-lines of ^{87}Rb,[44] which gives rise to $\kappa < 0$. Consequently, the atoms are high-field seeking and trapped in the focus point where the intensity is largest.

In the presence of the linear gravitational potential $V_g(z) = mgz$ with $g > 0$, the atoms are sagged downward out of the focus. The minimum of the total potential $V(\mathbf{x}) = V_{OD}(\mathbf{x}) + V_g(z)$ is now located at $(0, 0, z_0)$ with

$$z_0 = -\frac{1}{2}w\sqrt{-W_0\left(-\frac{g^2m^2\pi^2w^6}{\hbar^2\kappa^2P^2}\right)}, \tag{D3}$$

where $W_0(x)$ is the Lambert function. Note that the minimum vanishes at $g^2m^2\pi^2w^6/(\hbar^2\kappa^2P^2) \geq 1/\mathrm{e}$. Expanding the potential up to the second order at this point yields the trap frequencies

$$\omega_{x,y} = \sqrt{\frac{\hbar\kappa P}{2\pi m w^4 R^2}(2z_0^2-2R^2-w^2)}\exp\left\{-\frac{z_0^2}{w^2}\right\} \tag{D4}$$

and

$$\omega_z = \sqrt{-2\frac{w^2-4z_0^2}{\pi m w^6}\hbar\kappa P}\exp\left\{-\frac{z_0^2}{w^2}\right\}. \tag{D5}$$

Expanding the potential up to higher orders gives the anharmonic terms $\alpha(z-z_0)^3$ and $\beta(z-z_0)^4$ with

$$\alpha = 4\frac{3w^2-4z_0^2}{3\pi w^8}z_0\hbar\kappa P\exp\left\{-2\frac{z_0^2}{w^2}\right\}, \tag{D6}$$

$$\beta = \frac{3w^4-24w^2z_0^2+16z_0^4}{3\pi w^{10}}\hbar\kappa P\exp\left\{-2\frac{z_0^2}{w^2}\right\}. \tag{D7}$$

APPENDIX E: ANHARMONIC OSCILLATOR

The period of a classical 1D finite motion in a potential $V(z)$ is given by[34]

$$\mathcal{T}(E) = \sqrt{2m}\int_{z_1(E)}^{z_2(E)}\frac{dz}{\sqrt{E-V(z)}}, \tag{E1}$$

where E is the energy and the integration takes place between the classical turning points $z_1(E)$ and $z_2(E)$. Inserting the potential $V(z) = m\omega_z^2z^2/2 + \alpha z^3 + \beta z^4$ and calculating the integral perturbatively for $|\alpha| \to 0$ and $|\beta| \to 0$, we obtain the asymptotic expansion as follows:

$$\omega \approx \omega_z + \omega_z\left(\frac{3}{2}\beta - \frac{15}{4}\frac{\alpha^2}{m\omega_z^2}\right)\frac{Z_0^2}{m\omega_z^2} \tag{E2}$$

for the frequency $\omega = 2\pi/\mathcal{T}$. Here, $Z_0 = \sqrt{2E/(m\omega_z^2)}$ is the classical turning point of the purely harmonic motion.

We use Eq. (E2) to motivate the fit models for the data shown in Fig. 4(b) where we plot the frequencies against the distance $\Delta z = |z_{0,1} - z_{0,2}|$ between the trap centers. Within the order, we are interested in, we can set $Z_0 = \Delta z$ in Eq. (E2). The data were obtained by moving the minimum $z_{0,2}$ while keeping $z_{0,1} \approx -13.72\,\mu$m constant. To motivate the model for fitting $\omega_{2,z}$, we, therefore, express the former as $z_{0,2}(\Delta z) = z_{0,1} + \Delta z$ and insert this into Eqs. (D5)–(D7). The results are used as ω_z, α, and β in Eq. (E2), which leads to a dependence of these quantities on Δz, i.e., we have $\omega_z(\Delta z)$, $\alpha(\Delta z)$, and $\beta(\Delta z)$. Expanding Eq. (E2) up to the second order in Δz provides a good approximation for our parameters and gives rise to a contribution that is linear in Δz. Consequently, we employ the fit model $\omega_{2,z} = k_1 + k_2\Delta z + k_3\Delta z^2$.

For fitting the frequency $\omega_{1,z}$, we have to come back to the trajectories of the wavepackets. When determining the frequency by starting the interferometer in state $|1\rangle$, the wavepackets move extensively in both traps. For this reason, we fit to same model as for $\omega_{2,z}$. Starting the interferometer in state $|2\rangle$ means that at $T = n\mathcal{T}_1$ the wavepackets only move in the trap of state $|1\rangle$. In this case, the fit model reads $\omega_{1,z} = k_1 + k_3\Delta z^2$ in direct analogy to Eq. (E2). Moreover, the coefficient k_3 of this last fit can be used to obtain the upper bounds $\alpha^2 < 4m^2\omega_z^3|k_3|/15$ and $|\beta| < 2m\omega_z|k_3|/3$ on the magnitudes α and β of the anharmonic terms. Note that this only works if the fit results in a negative k_3 and it is known from earlier modeling that $\beta < 0$.

APPENDIX F: FREQUENCY EXTRACTION FOR OPTICAL DIPOLE TRAP

We simulate the MZI inside the crossed optical dipole potential described in Appendix D by first determining the ground state using an imaginary time evolution and afterward propagating the wavefunction with a standard split-step method. The pulses are implemented using the respective unitary operations, Eqs. (A2) and (A3). Inserting the trap frequencies obtained by Taylor expansion into our analytic model reveals the intervals for T in which the resonances of the two traps are separated in the signal. Likewise, the model can be used to show that the small difference between the transversal trap frequencies does not have a significant impact on the signal of the MZI.

Figure 5 displays the results of our simulation for the case of $g_2 = 0.8g_E$ and starting the MZI either starting in state $|1\rangle$ (blue) or in state $|2\rangle$ (red). Since we are always recording the population of state $|2\rangle$, the former case results in minima instead of maxima. Without the influence of transversal breathing, we would expect the oscillating resonances to peak at $P_2(T) = 1$ [or $P_2(T) = 0$], cf. Fig. 2. Then, we could simulate the MZI again but with a pulse

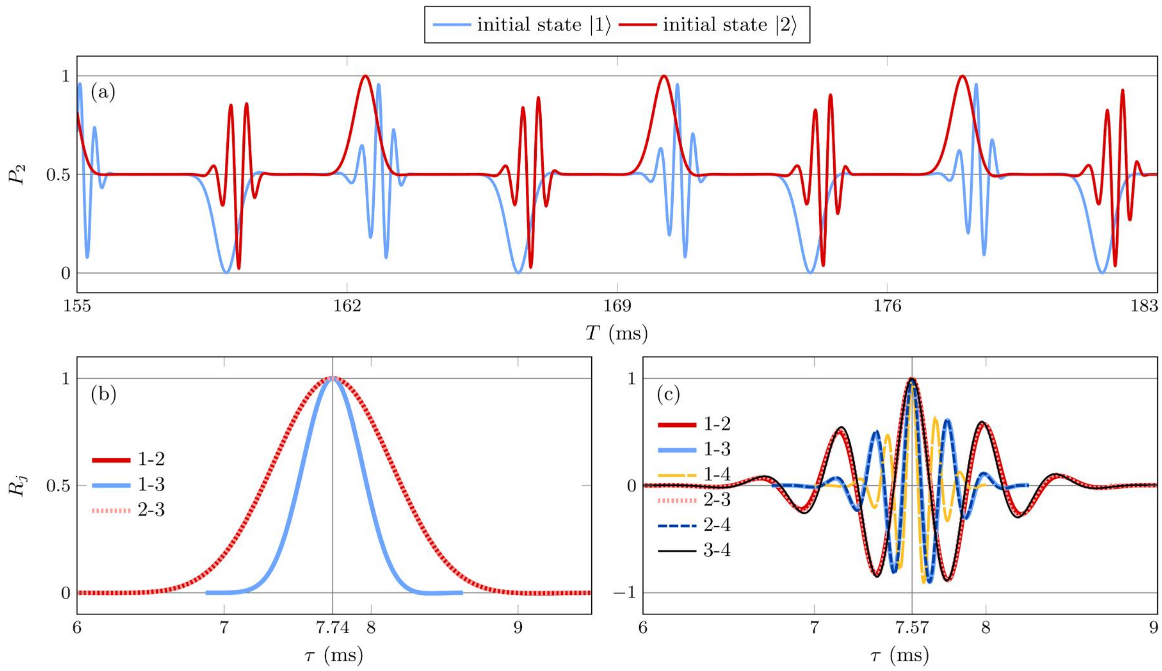

FIG. 5. (a) Interferometer signals P_2 as a function of the time between the pulses T obtained by simulating the MZI in a crossed optical dipole trap with $g_2 = 0.8g_E$ as discussed in Sec. V ($\Delta\Phi_P = 0$). (b) Cross-correlations R_j as a function of the delay τ for all combinations of the quasi-Gaussian resonances in the red curve of (a). The legend states the combination of resonances counting from left to right. (c) Same as (b) but for the oscillating resonances.

phase contribution of $\Delta\Phi_P = \pi/2$ and use the extraction scheme discussed in Sec. II. However, the anharmonicities of the optical dipole potential lead to new contributions to the phase of the interferometer $\varphi(T)$. Consequently, we face a similar problem as with transversal breathing, which is that $\varphi(T) \neq 0$ when T equals the period of the motion.

Since the signal is essentially a combination of two periodic processes, other methods to extract the periods can be used. Here, we apply the second method mentioned in Sec. IV, which is determining the shift that maximizes the overlap between resonances of the same type. As preparation, we split the signal into the individual resonances and shift them by 0.5. For each type of resonance (quasi-Gaussian or oscillating), a normalized cross-correlation

$$R_j(\tau) = \frac{\int \mathrm{d}T\, f(T) g(T + j\tau)}{\sqrt{\left[\int \mathrm{d}T\, f^2(T)\right]\left[\int \mathrm{d}T\, g^2(T)\right]}} \tag{F1}$$

is calculated between all possible combinations of individual resonances. The integer j is set to the number of periods in which the resonances are apart. Figure 5(b) shows the three possible cross-correlations for the quasi-Gaussian resonances of the red curve in Fig. 5(a), i.e., when starting the interferometer in state $|2\rangle$. Note that the correlation between the first and third resonance is more narrow because we set $j = 2$.

When starting the interferometer in state $|2\rangle$, the quasi-Gaussian resonances determine the period of the motion in the potential affecting state $|1\rangle$. Hence, from the average delay $\tau \approx 7.738\,08$ ms at which the correlations in Fig. 5(b) peak, we obtain $\omega_{1,z} \approx 2\pi \times 129.231$ Hz. The process is repeated for the oscillating resonances, which yields the correlations in Fig. 5(c), an average peak delay of $\tau \approx 7.568\,88$ ms and frequency $\omega_{2,z} \approx 2\pi \times 132.12$ Hz.

REFERENCES

[1]L. Amico et al., AVS Quantum Sci. **3**, 039201 (2021).
[2]R. Dumke, T. Müther, M. Volk, W. Ertmer, and G. Birkl, Phys. Rev. Lett. **89**, 220402 (2002).
[3]T. Petrucciani, A. Santoni, C. Mazzinghi, D. Trypogeorgos, F. S. Cataliotti, M. Inguscio, G. Modugno, A. Smerzi, L. Pezzé et al., arXiv:2504.17391 (2025).
[4]V. Xu, M. Jaffe, C. D. Panda, S. L. Kristensen, L. W. Clark, and H. Müller, Science **366**, 745 (2019).
[5]C. D. Panda, M. Tao, J. Egelhoff, M. Ceja, V. Xu, and H. Müller, Nat. Phys. **20**, 1234 (2024).
[6]M. Gebbe, J.-N. Siemß, M. Gersemann, H. Müntinga, S. Herrmann, C. Lämmerzahl, H. Ahlers, N. Gaaloul, C. Schubert et al., Nat. Commun. **12**, 2544 (2021).
[7]M. Horikoshi and K. Nakagawa, Phys. Rev. Lett. **99**, 180401 (2007).
[8]J. H. T. Burke, B. Deissler, K. J. Hughes, and C. A. Sackett, Phys. Rev. A **78**, 023619 (2008).
[9]R. E. Sapiro, R. Zhang, and G. Raithel, Phys. Rev. A **79**, 043630 (2009).
[10]G. D. McDonald, H. Keal, P. A. Altin, J. E. Debs, S. Bennetts, C. C. N. Kuhn, K. S. Hardman, M. T. Johnsson, J. D. Close et al., Phys. Rev. A **87**, 013632 (2013).
[11]G. D. McDonald, C. C. N. Kuhn, S. Bennetts, J. E. Debs, K. S. Hardman, M. Johnsson, J. D. Close, and N. P. Robins, Phys. Rev. A **88**, 053620 (2013).
[12]L. Masi, T. Petrucciani, A. Burchianti, C. Fort, M. Inguscio, L. Marconi, G. Modugno, N. Preti, D. Trypogeorgos et al., Phys. Rev. Res. **3**, 043188 (2021).
[13]E. R. Moan, R. A. Horne, T. Arpornthip, Z. Luo, A. J. Fallon, S. J. Berl, and C. A. Sackett, Phys. Rev. Lett. **124**, 120403 (2020).

[14]K. A. Krzyzanowska, J. Ferreras, C. Ryu, E. C. Samson, and M. G. Boshier, Phys. Rev. A **108**, 043305 (2023).
[15]M. M. Beydler, E. R. Moan, Z. Luo, Z. Chu, and C. A. Sackett, AVS Quantum Sci. **6**, 014401 (2024).
[16]Y. Balland, L. Absil, and F. Pereira Dos Santos, Phys. Rev. Lett. **133**, 113403 (2024).
[17]R. Grimm, M. Weidemüller, and Y. B. Ovchinnikov, in *Advances in Atomic, Molecular, and Optical Physics*, edited by B. Bederson and H. Walther (Academic Press, San Diego, CA, 2000), Vol. 42, pp. 95–170.
[18]C. J. Foot, *Atomic Physics* (Oxford University Press, Oxford, 2011).
[19]R. Folman, P. Krüger, J. Schmiedmayer, J. Denschlag, and C. Henkel, in *Advances in Atomic, Molecular, and Optical Physics*, edited by B. Bederson and H. Walther (Academic Press, San Diego, CA, 2002), Vol. 48, pp. 263–356.
[20]W. Lewoczko-Adamczyk, "Bose-Einstein condensation in microgravity," Ph.D. thesis (Humboldt-Universität zu Berlin, 2009).
[21]M. Keil, O. Amit, S. Zhou, D. Groswasser, Y. Japha, and R. Folman, J. Mod. Opt. **63**, 1840 (2016).
[22]R. A. Horne and C. A. Sackett, Rev. Sci. Instrum. **88**, 013102 (2017).
[23]D. Pfeiffer, L. Lind, J. Küber, F. Schmaltz, A. Turpin, V. Ahufinger, J. Mompart, and G. Birkl, Phys. Rev. A **108**, 053320 (2023).
[24]R. Jáuregui, Phys. Rev. A **64**, 053408 (2001).
[25]G. Moon, M.-S. Heo, Y. Kim, H.-R. Noh, and W. Jhe, Phys. Rev. A **81**, 033425 (2010).
[26]T. Lauber, J. Küber, O. Wille, and G. Birkl, Phys. Rev. A **84**, 043641 (2011).
[27]V. Makhalov, K. Martiyanov, T. Barmashova, and A. Turlapov, Phys. Lett. A **379**, 327 (2015).
[28]M. Olshanii, Phys. Rev. Lett. **81**, 938 (1998).
[29]T. Bergeman, M. G. Moore, and M. Olshanii, Phys. Rev. Lett. **91**, 163201 (2003).
[30]D. S. Petrov, M. Holzmann, and G. V. Shlyapnikov, Phys. Rev. Lett. **84**, 2551 (2000).
[31]T. Busch, B.-G. Englert, K. Rzążewski, and M. Wilkens, Found. Phys. **28**, 549 (1998).
[32]F. Haas, J. M. F. Bassalo, D. G. Da Silva, A. B. Nassar, and M. Cattani, Int. J. Theor. Phys. **52**, 88 (2013).
[33]Technically, a closed interferometer requires that the wavepackets have perfect overlap in both position and momentum space, which is satisfied in our case when $q_{\mathrm{u}}(2\mathcal{T}_\alpha) = q_{\mathrm{l}}(2\mathcal{T}_\alpha)$ and $\sigma_{\mathrm{u}}(2\mathcal{T}_\alpha) = \sigma_{\mathrm{l}}(2\mathcal{T}_\alpha)$, simultaneously.
[34]L. D. Landau and E. M. Lifshitz, *Mechanics* (Butterworth-Heinemann, Oxford, 1976).
[35]G. Afek, J. Coslovsky, A. Mil, and N. Davidson, Phys. Rev. A **96**, 043831 (2017).
[36]If the force is not aligned with a principal axis, all three center-of-mass motions are excited when the atoms are transferred to the other trap. In the general case where the trap frequencies of the three one dimensional traps have no common multiple, the atoms then orbit around their starting position and never come back.
[37]R. H. Leonard and C. A. Sackett, Phys. Rev. A **86**, 043613 (2012).
[38]W. LaRow, M. Edwards, and C. A. Sackett, Phys. Rev. A **111**, 033315 (2025).
[39]D. Steiner, Y. Y. Fein, G. Meier, S. Lindner, P. Juschitz, M. A. Ciampini, M. Aspelmeyer, and N. Kiesel, Appl. Phys. Lett. **127**, 191103 (2025).
[40]H. Ammann and N. Christensen, Phys. Rev. Lett. **78**, 2088 (1997).
[41]S. Pandey, H. Mas, G. Vasilakis, and W. von Klitzing, Phys. Rev. Lett. **126**, 170402 (2021).
[42]*Atom Interferometry: Proceedings of the International School of Physics "Enrico Fermi,"* edited by G. M. Tino and M. A. Kasevich (IOS Press, Amsterdam, 2014), Vol. 188.
[43]M. Krstajić, J. Kučera, L. R. Hofer, G. Lamb, P. Juhász, and R. P. Smith, Phys. Rev. A **111**, L051303 (2025).
[44]D. A. Steck, "Rubidium 87 D line data," available online at https://steck.us/alkalidata/rubidium87numbers.1.6.pdf (retrieved 1 February 2026).